RSC Advances

ROYAL SOCIETY OF CHEMISTRY

www.rsc.org/advances

Journal Name

ARTICLE

Structure, luminescence properties and energy transfer behavior of color-adjustable $Sr_3Gd_2(Si_3O_9)_2$:Ce^{3+}, Tb^{3+}/Mn^{2+} phosphors

Received 00th January 20xx,
Accepted 00th January 20xx

DOI: 10.1039/x0xx00000x

www.rsc.org/

Yingli Zhu[a, b], Yujun Liang[a, b,*] Mengfei Zhang[a, b], Miaohui Tong[a, b], Guogang Li[a, b], Song Wang[c]

A series of single-phased and emission-tunable $Sr_3Gd_2(Si_3O_9)_2$ (SGSO):Ce^{3+}, Tb^{3+}/Mn^{2+} phosphors have been successfully prepared via solid-state reaction, and the crystal structures, luminescence properties, energy transfer of Ce^{3+} → Tb^{3+} and Ce^{3+} → Mn^{2+}, color tuning and thermally stability were systematically investigated respectively. The energy transfer from Ce^{3+} to Tb^{3+} or Mn^{2+} ions were deduced from the spectral overlap between the Ce^{3+} emission and Tb^{3+}/Mn^{2+} excitation spectra. The energy transfer mechanisms of Ce^{3+} → Tb^{3+} and Ce^{3+} → Mn^{2+} in the host were verified to be a dipole–quadrupole interaction and dipole–dipole interaction, respectively, which made the emission color shift from blue to green and near white with the corresponding Commission Internationale deL'Eclairage (CIE) chromaticity coordinate from (0.174, 0.060) to (0.286, 0.615) and (0.319, 0.367), respectively. The good thermal stability of SGSO:0.26Ce^{3+}, 0.60Tb^{3+} and SGSO:0.26Ce^{3+}, 0.45Mn^{2+} samples showed about 72.3% and 86.1% at 150 °C of its initial emission intensity at room temperature due to the different energy transfer efficiency through Ce^{3+} → Tb^{3+} and Ce^{3+} → Mn^{2+}. The maximum quantum yields (QYs) of as-prepared SGSO:0.26Ce^{3+}, 0.10Tb^{3+} and SGSO:0.26Ce^{3+}, 0.57Mn^{2+} phosphors could reach 80.2% and 62.4%, respectively. All these properties indicate that the SGSO:Ce^{3+}, Tb^{3+}/Mn^{2+} phosphors have potential applications as ultraviolet-convertible phosphors.

1. Introduction

In recent years, most of the interest in luminescent rare-earth ions has concentrated on the single-phased multi-color emission phosphors.[1-3] Due to their unique properties including but not limited to stability of color temperature, good color rendering index and low cost, single-phased multi-color emission phosphors are the key of designing novel high-performance phosphors for the indispensable solid-state light source of phosphor-converted devices, such as fluorescence lamps, white light emitting diodes (WLEDs), and long-lasting phosphorescence materials, and so on.[4-6]

To generate multi-color emission from single-composition phosphors, two strategies have generally been adopted to modify the phosphors. One of the strategies is a modification of the composition of one activator ion doped the host by creating additional "sites" for this ion with another shift emission while retaining the first emission in the same host.[7,8] For example, the emission of Ce^{3+} in $Lu_2CaMg_2Si_3O_{12}$ can be strongly red-shifted when there is a larger crystal field splitting of the two lowest-energy 5*d* levels, or creating additional sites for Ce^{3+} with red emission via incorporating Si^{4+}-N^{3+} into the YAG:Ce^{3+} lattice.[9,10] Another approach leading to multi-color emission in a single host is by co-doping sensitizer and activator into a crystalline matrix, using the principle of energy transfer from sensitizer to activator[11], such as Eu^{2+}/Mn^{2+}, Eu^{2+}/Tb^{3+}, Ce^{3+}/Eu^{2+} Ce^{3+}/Mn^{2+} and Ce^{3+}/Tb^{3+}, which have been investigated in many hosts. For instance, $La_6Ba_4(SiO_4)_6F_2$:Ce^{3+}, Tb^{3+},[12] $Na_2CaMg(PO_4)_2$:Eu^{2+}, Mn^{2+},[13] $Ca_3Si_2O_7$:Ce^{3+}, Eu^{2+},[14] $Na_2Ca_4(PO_4)_3F$:Eu^{2+}, Tb^{3+},[15] $Sr_2MgSi_2O_7$:Eu^{2+}, Tb^{3+},[16] $NaBa_4(BO_3)_3$:Ce^{3+}, Tb^{3+},[17] $Y_4Si_2O_7N_2$:Ce^{3+}, Tb^{3+},[18] $Sr_7La_3[(PO_4)_{2.5}(SiO_4)_3(BO_4)_{0.5}](BO_2)$:$Ce^{3+}$, Mn^{2+},[19] $Na_4Ca_4Si_6O_{18}$:Ce^{3+}, Mn^{2+}.[20]

Incorporating two different luminescent centers into the host is the most effective way to broaden the applicability of inorganic phosphors. Because the Ce^{3+} ion commonly shows efficient broad band emission due to the 4*f*–5*d* parity allowed electric dipole transition, and it has a larger Stokes shift than those of the other RE ions owing to the extended radial wave functions of the 5*d* state.[21] The Ce^{3+} ion can act as an efficient sensitizer by transferring a part of its excitation energy to activators, which not only improves the photoluminescence of activator ions but also realizes multicolor-tunable emission in a single host. Recently, many researchers have studied the energy transfer mechanism from Ce^{3+} to Tb^{3+} or Mn^{2+} in some proper

[a] Engineering Research Center of Nano-Geomaterials of Ministry of Education, China University of Geosciences, Wuhan 430074, People's Republic of China
[b] Faculty of Materials Science and Chemistry, China University of Geosciences, Wuhan 430074, People's Republic of China
[c] Hubei Key Laboratory of Low Dimensional Optoelectronic Materials and Devices, Hubei University of Arts and Science, Xiangyang, 441053, Hubei, China
† Footnotes relating to the title and/or authors should appear here.
Electronic Supplementary Information (ESI) available: [details of any supplementary information available should be included here]. See DOI: 10.1039/x0xx00000x

single host lattice for UV-based WLED application, such as $KGdF_4:Ce^{3+}$, Tb^{3+},[22] $CaAl_2SiO_6:Ce^{3+}$, Tb^{3+},[23] $La_5Si_2BO_{13}:Ce^{3+}$, Mn^{2+},[24] $KBaY(BO_3)_2:Ce^{3+}$, Mn^{2+},[25] and $Ca_3Al_2O_6:Ce^{3+}$, Tb^{3+}/Mn^{2+}.[26] In these hosts, when Tb^{3+} or Mn^{2+} ions are singly doped, the luminescent properties are undesirable upon UV light excitation due to the $4f$–$4f$ weak absorption of Tb^{3+} and the forbidden $^4T_1 \rightarrow {}^6A_1$ transition of Mn^{2+}.[27] By the introduction of an efficient sensitizer of Ce^{3+}, the energy would be transferred from the 5D level of Ce^{3+} to the $^5D_{3,4}$ level of Tb^{3+} or to the 4G level of Mn^{2+}, which improve the luminescence efficiency of Tb^{3+} or Mn^{2+} ion.

Both one activator phosphors and co-doping sensitizer and activator phosphors can produce multi-color emission, however, one activator phosphors normally appeared lower CRI due to the different distribution of higher and lower energy sites for the same activator ions in the host. Considering this problem and the advantages of the co-doping sensitizer and activator phosphors, we believe that the co-doping sensitizer and activator phosphors are the most reliable and economical way to achieve multi-color emission in one host.

Among manifold multi-color emission luminescent materials, silicates have been extensively studied as the satisfactory host lattices for phosphors owing to their outstanding thermal, chemical, mechanical stability and structural diversity. For instance $Ca_4Y_6(SiO_4)_6O:Ln^{3+}$ (Ln = Eu, Tb),[28] $CdSiO_3:Eu^{3+}$,[29] $BaZrSi_3O_9:Eu^{3+}$,[30] $Mg_2SiO_4:Tb^{3+}$,[31] $Ba_5Si_8O_{21}:Eu^{2+}$, Dy^{3+},[32] $CaAlSiN_3:Ce^{3+}$,[33] and so on have been reported recently. As a member of the silicate family, the cyclosilicates $Sr_3R_2(Si_3O_9)_2$ (R = Y, Eu–Lu), has been synthesized via a solid-state reaction by Alexander P. Tyutyunnik. [34] The synthesized $Sr_3R_2(Si_3O_9)_2$ compounds corresponds to the formula of $Ca_3Y_2(Si_3O_9)_2$, which derived from a wadeite α-$CaSiO_3$ (pseudowollastonite, a high-temperature polymorph of $CaSiO_3$).[35,36] The $Sr_3R_2(Si_3O_9)_2$ oxides crystallize in the monoclinic crystal system (S.G. C2/c, Z = 4) and have a morphotropic phase transition between Er and Tm compounds followed by a step-like change of the unit cell constants. There are three Sr/R sites coordinated by 8, 7 and 6 oxygen atoms for the doped ions to occupy which attracting much attention. Tyutyunnik also investigated the photoluminescence properties and applications in UV-LEDs of $Sr_3Y_2(Si_3O_9)_2:Eu^{3+}$ phosphor. It showed superior luminescence property in the orange-red spectral region with multiband photoluminescence emission under UV excitation, which was efficient to generate white light emitting. As one of the new cyclosilicates $Sr_3R_2(Si_3O_9)_2$ (R = Y, Eu–Lu), $Sr_3Gd_2(Si_3O_9)_2$ (SGSO) host material has been determined. However, to the best of our knowledge, there is no report concentrating on the luminescent properties of co-doped with multiple rare earth ions (Ce^{3+}, Tb^{3+}/Mn^{2+}) and the energy transfer between them in the host of SGSO. In this study, we firstly investigated the luminescence properties, energy transfer, color tunability and thermal stability of a full-color emitting phosphor. The results reveal that the as-prepared $SGSO:Ce^{3+}$, Tb^{3+}/Mn^{2+} phosphors exhibit intense adjustable blue/green/white emission with high quantum yields (QYs) and thermal stability, and the energy transfer from Ce^{3+} to Tb^{3+} or Mn^{2+} with a high efficiency is found and studied in details.

2. Experimental

2.1 Materials and Synthesis

A series of polycrystalline $Sr_{3-z}Gd_{2-x-y}(Si_3O_9)_2:xCe^{3+}$, yTb^{3+}/zMn^{2+} powder samples were prepared via conventional high temperature solid state reaction process. On the basis of the similar effective ionic radius and valence of the cations, we suggested that Ce^{3+}/Tb^{3+} and Mn^{2+} ions prefer to occupy Gd^{3+} and Sr^{2+} sites in the host of SGSO, respectively. In order to facilitate the expression, in the following sections $Sr_{3-z}Gd_{2-x-y}(Si_3O_9)_2:xCe^{3+}$, yTb^{3+}/zMn^{2+} were abbreviated as $SGSO:xCe^{3+}$, yTb^{3+}/zMn^{2+} ($x/y/z$ represent mol% in this article). The starting materials, $SrCO_3$ (A.R.), Gd_2O_3 (A.R.), SiO_2 (A.R.), H_3BO_3 (A.R.), Tb_4O_7 (≥99.99%) and CeO_2 (≥99.99%) were thoroughly ground and mixed for 30 minutes with stoichiometric molar ratios in an agate mortar to form a homogeneous mixture. Then the mixtures were transferred into alumina crucibles and sintered at 1300°C for 4 h under a reducing atmosphere of 95%N_2-5%H_2 in a horizontal tube furnace. After the furnace slowly cooled to room temperature, the calcined products were ground again, yielding the final phosphor powders.

2.2 Characterization

The phase purity of the as-prepared samples was characterized by X-ray powder diffractometer (XRD) (Bruker D8 Focus, Bruker, Kalsruhe, Germany) with Ni-filtered Cu-Kα (λ = 1.540598 Å) radiation at 40 kV tube voltage and 40 mA tube current. The XRD data were collected in a 2θ range from 5° to 70°, with the continuous scan mode at the speed of 0.05 s per step with step size of 0.01°. The measurements of photoluminescence emission and photoluminescence excitation spectra were performed by using fluorescence spectrometer (Fluoromax-4P, Horiba Jobin Yvon, New Jersey, USA.) equipped with a 450 W xenon lamp as the excitation source and both excitation and emission spectra were set up to be 1.0 nm with the width of the monochromator slits adjusted as 0.50 nm. The photoluminescence decay curves were obtained from a Lecroy Wave Runner 6100 Digital Osilloscope (1 GHz) using a tunable laser (pulse width = 4 ns, gate = 50 ns) as the excitation (Continuum Sunlite OPO). The QYs were measured by absolute photoluminescence quantum yield measurement system C9920-02.

3. Results and Discussion

3.1 Phase Identification, XRD Refinement and Crystal Structure

The phase purity and crystal structure of the as-prepared samples were firstly identified by XRD. Fig. 1 shows the XRD patterns of the as-prepared $SGSO:0.26Ce^{3+}$, $0.40Tb^{3+}$, $SGSO:0.26Ce^{3+}$, $1.20Tb^{3+}$, $SGSO:0.26Ce^{3+}$, $1.60Tb^{3+}$, $SGSO:0.26Ce^{3+}$, $0.33Mn^{2+}$, $SGSO:0.26Ce^{3+}$, $0.57Mn^{2+}$ and the SGSO phase reported by Tyutyunnik[34] as a reference. All the diffraction peaks of the samples were well indexed to the reported $Sr_3Gd_2(Si_3O_9)_2$ phase, indicating that the obtained samples were single phase and the doped ions were completely dissolved in the SGSO host without inducing significant changes of the crystal structure. In addition, Fig. S1 (Supporting

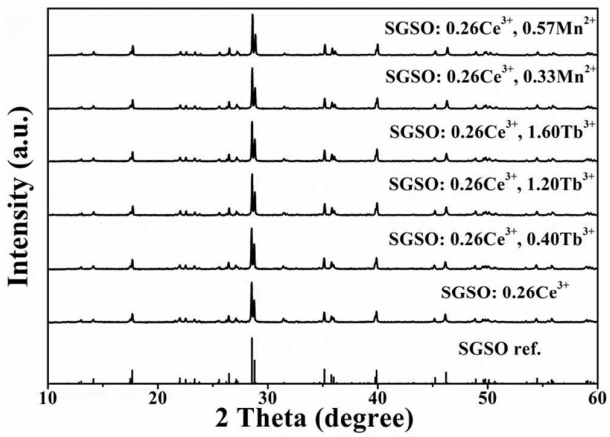

Fig. 1 XRD patterns of SGSO:0.26Ce^{3+}, SGSO:0.26Ce^{3+}, 0.40Tb^{3+}, SGSO:0.26Ce^{3+}, 1.20Tb^{3+}, SGSO:0.26Ce^{3+}, 1.60Tb^{3+}, SGSO:0.26Ce^{3+}, 0.33Mn^{2+}, SGSO:0.26Ce^{3+}, 0.57Mn^{2+} and the SGSO phase reported by A.P. Tyutyunnik as a reference.[34]

Information) presents the powder XRD patterns of SGSO:$x$$Ce^{3+}$ samples with the doping concentration of the Ce^{3+} ion ranging from 0.08 to 0.44. The patterns showed that no impurity phase can be detected and the studied samples were all pure SGSO phase. Fig. S1(b) presents partial enlarged details of XRD patterns of SGSO:$x$$Ce^{3+}$ (x = 0.08, 0.14, 0.20, 0.26, 0.32, 0.38, 0.44). An obvious red shifting of the major diffraction peak at $2\theta = 28.8°$ could be observed with the increase of the Ce^{3+} concentration.

In order to further understand the microstructure of the as-prepared samples, detailed Rietveld refinements were performed on the samples of SGSO:0.26Ce^{3+}, 0.60Tb^{3+} and SGSO:0.26Ce^{3+}, 0.33Mn^{2+}. The starting model was built with crystallographic data taken from Tyutyunnik et al.[34] Fig. 2 presents the results of the experimental, calculated, different XRD powder and Bragg positions for the Rietveld refinement of SGSO:0.26Ce^{3+}, 0.60Tb^{3+} and SGSO:0.26Ce^{3+}, 0.33Mn^{2+} at room temperature. Table 1 summarizes the final refined structural parameters, reliability factors which were from refined convergence and satisfied well with the reflection condition. It was found that the cell volume increased with the introduction of the Ce^{3+}, Tb^{3+} or Mn^{2+} than the undoped[34] which could be ascribed to the different ionic radii of the dopant ions compared with those of the SGSO host. All atom positions, fraction factors, occupation probability, thermal vibration parameters and selected interatomic distances of SGSO:0.26Ce^{3+}, 0.60Tb^{3+} sample are showed in Table S1 and Table S2. The above results confirmed the phase purity of the as-prepared samples.

SGSO has a monoclinic phase with space group $C2/c$ (15). The crystal structure of SGSO and the coordinated condition of Sr1/Gd1(8f), Sr2/Gd2(8f), Sr3/Gd3(4e) which are coordinated by 6, 7 and 8 oxygen atoms, respectively are depicted in Fig. 3. The structure of SGSO could be described as Sr/Gd atom layers and Si_3O_9 ring layers. Every SiO_4 tetrahedron shared two O atoms with other SiO_4 tetrahedra to construct a ternary Si_3O_9 ring connected by Sr/Gd atoms. Isolated Si_3O_9 rings were located in layers stacking with Sr/Gd layers along the [1 0 -1] direction. The ionic radius (Å) of Sr^{2+}, Gd^{3+}, Ce^{3+}, Tb^{3+} and Mn^{2+} for the given coordination

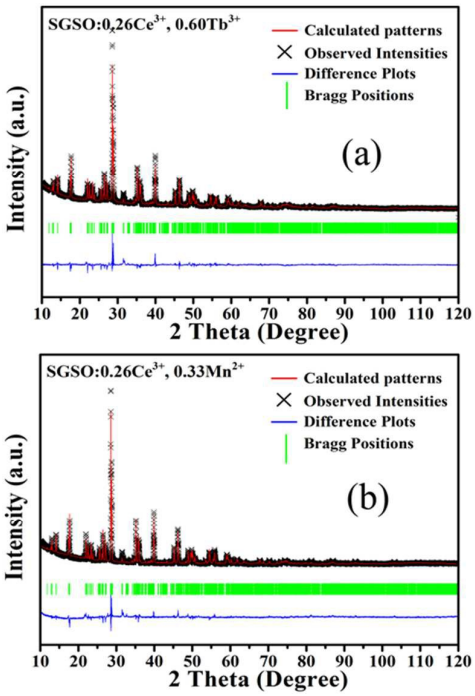

Fig. 2 Experimental (crosses) and calculated (red solid line) XRD patterns and their difference (blue solid line) for the Rietveld fit of SGSO:0.26Ce^{3+}, 0.60Tb^{3+} and SGSO:0.26Ce^{3+}, 0.33Mn^{2+} XRD patterns by the Fullprof program. The short vertical lines show the positions of Bragg reflections of the calculated pattern.

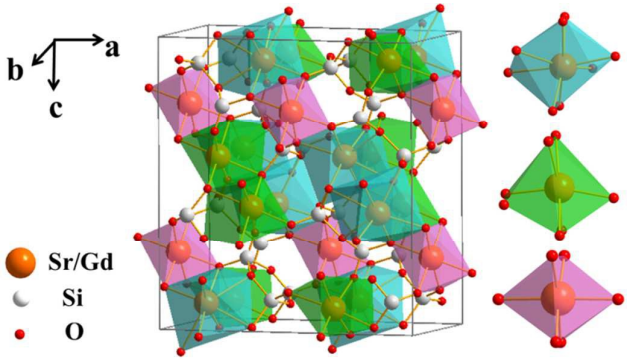

Fig. 3 Crystal structure schematic diagram of $Sr_3Gd_2(Si_3O_9)_2$.

number (CN) are presented in Table S3. On the basis of ionic radius and charge balance, the Ce^{3+}/Tb^{3+} and Mn^{2+} occupied the Gd^{3+} and Sr^{2+} site, respectively. Moreover, owing to the larger Ce^{3+} ions substituting for the smaller Gd^{3+} ions, the substitution led to the increasing of interplanar spacing (d) then the decreasing of diffraction angle (2θ). This matched well with the above X-ray powder diffraction results illustrated in Fig. S1. The similar phenomenon also existed in Fig. 1 of smaller Tb^{3+} or Mn^{2+} substituting for the larger Gd^{3+} and Sr^{2+} ions. It also verified the incorporation of Ce^{3+}, Tb^{3+} and Mn^{2+} into the lattice and the formation of solid solutions according to the Vegard rule.[37]

Table 1 Final refined structure parameters of SGSO:0.26Ce^{3+}, 0.60Tb^{3+} and SGSO:0.26Ce^{3+}, 0.33Mn^{2+} derived from the Fullprof refinement of X-ray diffraction data.

Formula	SGSO:0.26Ce^{3+}, 0.60Tb^{3+}	SGSO:0.26Ce^{3+}, 0.33Mn^{2+}
Crystal style	Monoclinic	Monoclinic
Space group	*C*2/c (15)	*C*2/c (15)
a(Å)	13.59469	13.59030
b(Å)	8.02849	8.01865
c(Å)	14.96769	14.96759
β°	89.60880	89.62453
V(Å^3)	1633.608	1631.071
R_{wp}(%)	4.38	4.42
R_p(%)	3.15	3.17
χ^2	2.93	5.91

3.2 Photoluminescence properties of SGSO:Ce^{3+}

Fig. 4(a) displays the excitation and emission spectra of as obtained SGSO:0.26Ce^{3+} phosphors. The excitation spectrum of SGSO:0.26Ce^{3+} showed two broad bands centered at 295 and 348 nm (the strongest) which were attributed to the electronic transitions from the ground state of Ce^{3+} to the crystal field splitting of *5d* states of Ce^{3+}, as shown in Fig. 4(a). Then excited by 348 nm, the emission spectrum showed an asymmetric broad band from 370 to 500 nm with the maximum value at 416 nm, which was attributed to the *5d*–*4f* transitions of Ce^{3+}, implying a possible spectral overlap generated from different luminescence centers. The emission spectrum of SGSO:0.26Ce^{3+} was decomposed into three Gaussian components with peaks at 398, 420 and 446 nm, respectively. These components could be ascribed to that the Ce^{3+} ions occupied three different sites in the SGSO host which was identified with the Sr/Gd sites coordinated by different number of O atoms. It contributed to the transition from the lowest *5d* excited state to the ground state of Ce^{3+} ions at three different Ce^{3+} luminescence centers. Fig. 4(b) exhibits the normalized emission spectra of SGSO:*x*Ce^{3+} samples with various Ce^{3+} contents (*x* = 0.08, 0.14, 0.20, 0.26, 0.32, 0.38, 0.44). An slight red shift could be observed due to the larger Ce^{3+} ions substituting for the smaller Gd^{3+} ions as a result of the electron atmosphere of Ce^{3+} being compressed. The dependence of the Ce^{3+} luminescence intensity on its doping concentration is also displayed in inset. The highest integrated emission intensity was noted at the Ce^{3+} concentration of *x* = 0.26, which was taken as the critical concentration. The emission intensity firstly increased with adding of doping Ce^{3+} ions concentration, reaching the optimum point, and then decreased with doping content due to the concentration quenching effect. Concentration quenching might occur because the excitation energy migrates about a large number of centers before being emitted at the high concentrations.

According to Van Uitert, the emission position of the Ce^{3+} ion was strongly dependent on its local environment, which was suggested to obey an empirical relation between the energetic position of the Ce^{3+} emission and the local environment in diverse

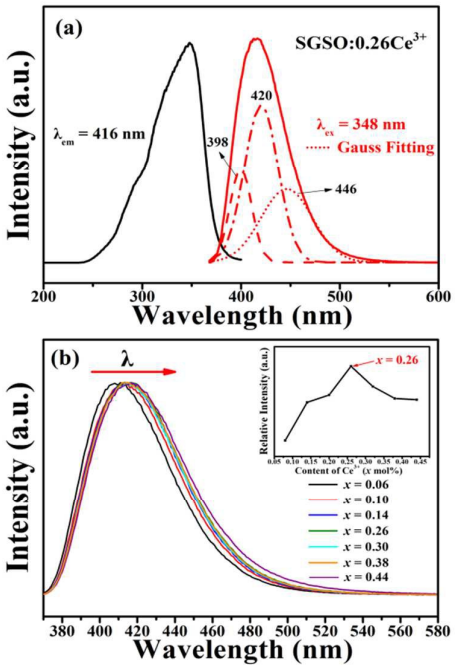

Fig. 4 (a) The excitation and emission spectra of SGSO:0.26Ce^{3+}, together with the Gaussian peaks fitting (three red dashed lines) of the emission spectrum. (b) The normalized emission spectra of SGSO:*x*Ce^{3+} (*x* = 0.08, 0.14, 0.20, 0.26, 0.32, 0.38, 0.44) under excitation at 348 nm. The inset is the relative intensity of Ce^{3+} concentration.

compounds by Van Uitert[38] as obeying:

$$\mathbf{E}(\mathbf{cm^{-1}}) = \mathbf{Q}^* \left[\mathbf{1} - \left(\frac{\mathbf{V}}{\mathbf{4}}\right)^{\frac{\mathbf{1}}{\mathbf{V}}} \times \mathbf{10}^{\frac{-(\mathbf{nE_a r})}{\mathbf{80}}} \right] \qquad (1)$$

In the above equation, **E** is the position for the rare-earth ion emission peak (cm^{-1}), $\mathbf{Q}^*$ is the position in energy for the lower d-band edge for the free ion ($\mathbf{Q}^*$ = 50000 cm^{-1} for Ce^{3+}), **V** is the valence of the active ion (**V** = 3 for Ce^{3+}), **n** is the number of anions in the immediate shell around the active ion, $\mathbf{E_a}$ is the electron affinity of the atoms that form anions (eV), and **r** is the radius of the host cation replaced by the Ce^{3+} ion (Å). Since $\mathbf{E_a}$ is constant in the same host, **V** = 3, $\mathbf{Q}^*$ = 50000 cm^{-1}, the value of **E** is directly proportional to the product of **n** and **r**. The expected value of **E** determined using above equation for Ce^{3+} substituting GdO_6 (n = 6, r = 1.05 Å), GdO_7 (n = 7, r = 1.00 Å) and GdO_8 (n = 8, r = 0.94 Å) was increased in turn. Therefore, we could draw the conclusion that the band centered at 398 nm was attributed to Ce^{3+} luminescence centers occupying the eight-coordination Sr1/Gd1 site, the band centered at 420 nm was assigned to Ce^{3+} ions occupying the Sr2/Gd2 site with seven-coordinated, and the band with peak at 446 nm belonged to Ce^{3+} luminescence centers occupying the six-coordinated Sr3/Gd3 site.

3.3 Photoluminescence properties and energy transfer of SGSO:Ce^{3+}, Tb^{3+}

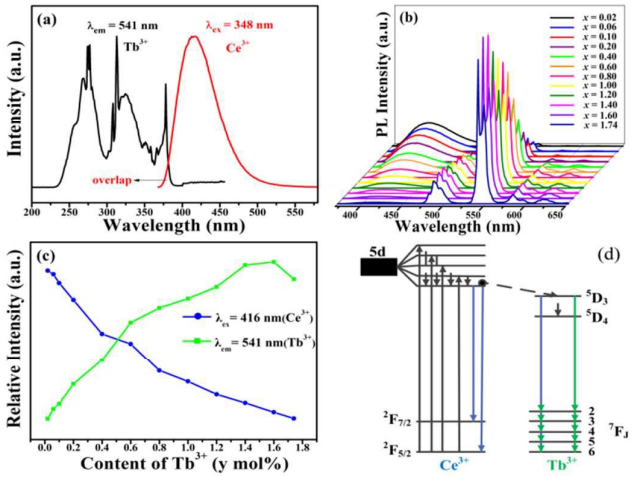

Fig. 5 (a) The spectral overlap between the emission band of Ce^{3+} and the excitation peaks of Tb^{3+} (b) The emission spectra of SGSO:0.26Ce^{3+}, $y$$Tb^{3+}$ (y = 0.02, 0.06, 0.10, 0.20, 0.40, 0.60, 0.80, 1.00, 1.20, 1.40, 1.60, 1.74) under excitation at 348 nm. (c) The emission relative intensity of Ce^{3+} and Tb^{3+} (d) The energy level diagram of Ce^{3+}, Tb^{3+}.

The excitation and emission spectra of the Tb^{3+} singly doped SGSO matrix were studied in our other work. Here, the Ce^{3+} → Tb^{3+} energy transfer in SGSO:Ce^{3+}, Tb^{3+} system was investigated in detail. Fig. 5(a) demonstrates a significant overlap between the emission band of Ce^{3+} and the excitation band of Tb^{3+}. According to the energy transfer formula, which was given by Dexter[39] is expressed as the following equation:

$$P_{SA} = \frac{2\pi}{h}|\langle S, A^*|H_{SA}|S^*, A\rangle|^2 \int g_S(E) g_A(E) dE \qquad (2)$$

where P_{SA} is energy transfer rate and H_{SA} is the interaction Hamiltonian that mediates energy transfer from the excited sensitizers to the unexcited activators. The matrix element indicates the interaction between the initial state $|S^*, A\rangle$ and the final state $\langle S, A^*|$. The integral represents the spectral overlap between the emission spectrum of the sensitizers and the excitation spectrum of the activators. From the observed spectral overlap between the emission band of Ce^{3+} and the excitation peaks of Tb^{3+}, we could conclude from above equation that a possible resonance type energy transfer might occur in SGSO:Ce^{3+}, Tb^{3+} samples.[2]

Fig. 5(b) shows a series of emission spectra for SGSO:0.26Ce^{3+}, $y$$Tb^{3+}$ (y = 0.02, 0.06, 0.10, 0.20, 0.40, 0.60, 0.80, 1.00, 1.20, 1.40, 1.60, 1.74) under UV excitation (λ_{ex} = 348 nm). It could be revealed from Fig. 5(c) that the emission intensity of Ce^{3+} gradually decreased while the emission intensity of Tb^{3+} gradually increased with the increase of Tb^{3+} concentration, making further confirmations on the existence of Ce^{3+} → Tb^{3+} energy transfer in SGSO:Ce^{3+}, Tb^{3+}. The Tb^{3+} emission intensity was saturated when the Tb^{3+} dopant content (y) was above 1.60. This was attributed to the concentration quenching effect, which occurred when the activator concentration was high. To comprehend the process of energy transfer in the co-doped SGSO phosphors more clearly, the energy level diagram is given by the inset in Fig. 5(d). In SGSO:Ce^{3+}, Tb^{3+} phosphor with exciting Ce^{3+}, electrons were excited from the ground state, $^2F_{5/2}$, to the 5*d* excited state of Ce^{3+} simultaneously due to the level of 5*d* excited state of Ce^{3+} was close to the level of $^5D_4$ of Tb^{3+}, there was a certain probability that the energy transfer from 5*d* excited state of Ce^{3+} to $^5D_4$ of Tb^{3+} through relaxation and nonradiative progress. The transitions of $^5D_4$-$^7F_5$ of Tb^{3+} led to release 541 nm photons.[27]

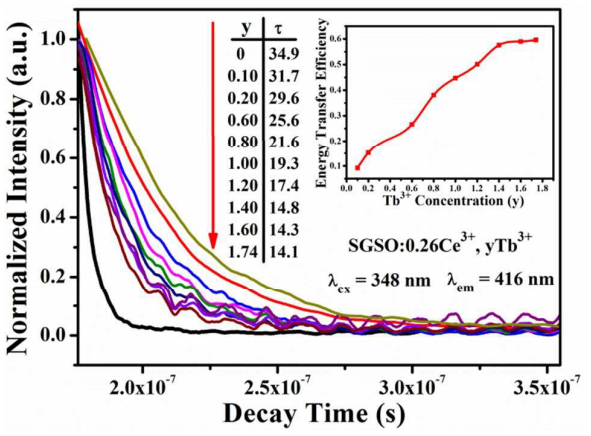

Fig. 6 Decay curves of Ce^{3+} emission monitored at 416 nm for SGSO:0.26Ce^{3+}, $y$$Tb^{3+}$ (y = 0, 0.10, 0.20, 0.60, 0.80, 1.00, 1.20, 1.40, 1.60, 1.74) under excitation at 348 nm. The inset shows the dependence of energy transfer efficiency (η_T) on the Tb^{3+} content.

In order to further detect the Ce^{3+} → Tb^{3+} energy transfer process in the SGSO host lattice, the lifetime dependence of Ce^{3+} on the concentration of Tb^{3+} in SGSO:0.26Ce^{3+}, $y$$Tb^{3+}$ (y = 0, 0.10, 0.20, 0.60, 0.80, 1.00, 1.20, 1.40, 1.60, 1.74) phosphors were measured at 348 nm excited and monitored at 416 nm, the decay curves are shown in Fig. 6. Since there were three Ce^{3+} luminescent centers in the SGSO host, the decay curves were successfully fitted using the following three exponential equation:[40,41]

$$I(t) = I_0 + A_1\exp(-t/\tau_1) + A_2\exp(-t/\tau_2) + A_3\exp(-t/\tau_3) \qquad (3)$$

where $I(t)$ and I_0 are the luminescence intensities at times t; A_1, $A_2$and A_3 are fitting constants and τ_1, τ_2 and τ_3 are the decay times for the exponential components. Using these parameters, the average decay times (τ^*) can be determined by the formula as follows:[42]

$$\tau^* = \frac{A_1\tau_1^2 + A_2\tau_2^2 + A_3\tau_3^2}{A_1\tau_1 + A_2\tau_2 + A_3\tau_3} \qquad (4)$$

The average decay times τ were calculated to be 34.9, 31.7, 29.6, 25.6, 21.6, 19.3, 17.4, 14.8, 14.3 and 14.1 ns for SGSO:0.26Ce^{3+}, $y$$Tb^{3+}$ with y = 0, 0.10, 0.20, 0.60, 0.80, 1.00, 1.20, 1.40, 1.60 and 1.74, respectively.

The energy transfer efficiency (η_T) could be calculated using the following equation by Paulose et al.[43]

$$\eta_T = 1 - \frac{\tau_S}{\tau_{S0}} \qquad (5)$$

where τ_{S0} and τ_S stand for the lifetimes of Ce^{3+} in the absence and the presence of Tb^{3+}, respectively. Results showed that the η_T values from Ce^{3+} to Tb^{3+} for SGSO:0.26Ce^{3+}, $y$$Tb^{3+}$ (y = 0.10, 0.20, 0.60, 0.80, 1.00, 1.20, 1.40, 1.60, 1.74) were calculated to be 9.2%, 15.2%, 26.6%, 38.1%, 44.7%, 50.1%, 57.6%, 59.0%, 59.6% respectively. The inset of Fig. 6 shows the dependence of energy transfer efficiency (η_T) on the Tb^{3+} content. All results above proved that the energy transfer process from Ce^{3+} to Tb^{3+} in the SGSO host is very efficient.

In order to understand the energy transfer mechanism of SGSO:Ce^{3+}, Tb^{3+}, it was available to know the critical distance R_C, which is defined as the distance for which the probability of transfer equals to the probability of radiative emission of energy donator by the ion of Ce^{3+} in this system.[44] In this passage, the R_C was first calculated by using the concentration quenching method, where the critical distance R_C between Ce^{3+} and Tb^{3+} could be estimated by the following formula given by Blasse.[39]

$$R_C = 2\left[\frac{3V}{4\pi X_C N}\right]^{1/3} \qquad (6)$$

where V is the volume of the unit cell, and N is the number of cations in the unit cell. X_C is the critical concentration at which the luminescence intensity of Ce^{3+} as a sensitizer was half of that in the sample in the absence of Tb^{3+} as an activator, that is to say, X_C occurred when η_T = 0.5. In this case, N = 4, V = 1633.608 Å^3 and X_C was 0.60 in the SGSO:Ce^{3+}, Tb^{3+} system. Accordingly, the critical distance R_C was calculated to be about 10.91 Å for Ce^{3+} and Tb^{3+} in SGSO host.

Exchange interactions and multipolar interactions are the two main aspects responsible for the resonant energy transfer mechanism. In general, if energy transfer results from the exchange interactions, the critical distance (R_C) between the sensitizer and activator should be shorter than 4 Å. In this system, the critical distance of energy transfer (R_C) was relatively long, the exchange interaction could be disregarded.[45] In accordance with Dexter's energy transfer expressions of exchange and multipolar interaction and Reisfeld's approximation, the following relationship could be formed as:[39,46]

$$I_{S0}/I_S \propto y^{n/3} \qquad (7)$$

where y is the concentration of Tb^{3+}, I_{S0} and I_S are the luminescence intensity of a sensitizer (Ce^{3+}) in the absence and presence of an activator (Tb^{3+}), respectively. $I_{S0}/I_S \propto y^{n/3}$, with n = 6, 8, and 10 corresponds to dipole-dipole (*d*–*d*), dipole-quadrupole (*d*–*q*) and quadrupole-quadrupole (*q*–*q*) interactions, respectively.[47] The relationships between I_{S0}/I_S with $y^{n/3}$ are illustrated in Fig. 7(a)-(c). The linear relationship reached the optimal one for $I_{S0}/I_S \propto y^{n/3}$ by comparing the fitting factors of *R* values in Fig. 7(b), implying that energy transfer from Ce^{3+} to Tb^{3+} occurred via the dipole−quadrupole interactions.

Considering the dipole–quadrupole interaction, the critical distance from the sensitizer to the activator could also be calculated by the spectral overlap method, as simplified expression by:[26]

$$R_C^8 = 3.024\times10^{12}\lambda_S^2 f_q \int \frac{F_S(E)F_A(E)dE}{E^4} \qquad (8)$$

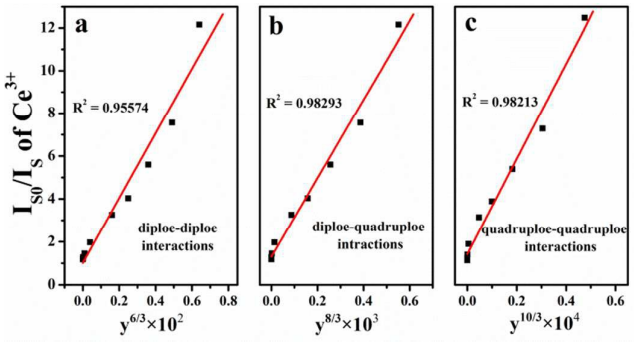

Fig. 7 Dependence of I_{S0}/I_S of Ce^{3+} in SGSO:0.26Ce^{3+}, $y$$Tb^{3+}$ (y = 0.02, 0.06, 0.10, 0.20, 0.40, 0.60, 0.80, 1.00, 1.20, 1.40, 1.60, 1.74) samples, (a) $y^{6/3}$, (b) $y^{8/3}$ and (c) $y^{10/3}$.

where f_q is the oscillator strength of the electric quadrupole transition of the activator ion (Tb^{3+}), λ_S (Å) is the wavelength corresponding to the strongest emission peak of the sensitizer, and E is the energy (eV) corresponding to the largest emission wavelength. $\int F_S(E)F_A(E)dE/E^4$ represents the spectral overlap between the normalized emission spectrum, $F_S(E)$, of the Ce^{3+} and the excitation spectrum, $F_A(E)$, of Tb^{3+}. However, the oscillator strength of the Tb^{3+} quadrupole transition (f_q) did not obtained up to now. It was suggested by Verstegen et al. that the ratio f_q/f_d is about 1×10^{-2} to 1×10^{-3} when f_d applies to a forbidden dipole transition.[48] f_d is the oscillator strength of the involved dipole absorption transition of the activator. In our case, using above equation with λ_S = 4140 Å, f_q= 10^{-2}–10^{-3} f_d, f_d of the Tb^{3+} transition is 0.3×10^{-6}, $\int F_S(E)F_A(E)dE/E^4$ was calculated to be about 0.01211 eV^{-5}, and the critical distance (R_C) was calculated to be 10.82−14.43 Å for the dipole-quadrupole interaction. This agreed approximately with the concentration-quenching method (10.91 Å), which further concluded that the mechanism of energy transfer from the Ce^{3+} to Tb^{3+} ions was mainly due to a dipole−quadrupole interaction.

3.4 Photoluminescence properties and energy transfer of SGSO:Ce^{3+}, Mn^{2+}

It is known that Mn^{2+} generally shows a broad emission band because of the $^4T_1 - {}^6A_1$ transition within the 3d shell, in which the electrons are strongly coupled to lattice vibrations and are affected by the crystal field strength and site symmetry.[49] The emission color of Mn^{2+} can vary from green under strong crystal field to orange/red under weak crystal field. However, the excitation transitions of Mn^{2+} are difficult to pump and the emission intensity is very weak due to the forbidden *d*-*d* transitions. In order to enhance the absorption and emission of Mn^{2+}, we designed the $Ce^{3+} \rightarrow Mn^{2+}$ energy transfer in SGSO host and studied the luminescence properties and energy transfer of SGSO:Ce^{3+}, Mn^{2+} samples in detail. As shown in Fig. 8, the emission band of Ce^{3+} and the excitation peaks of Mn^{2+} were presented. The excitation peaks of Mn^{2+} consisted of two parts: one part included two sharp peaks at 274 and 313 nm, corresponding to the $^8S \rightarrow {}^6I$ and $^8S \rightarrow {}^6P$ transitions of Gd^{3+} ions in the host, respectively;[50] and the other part contained several peaks located at 344, 361, 406, 449, and 468 nm corresponding to the transitions of

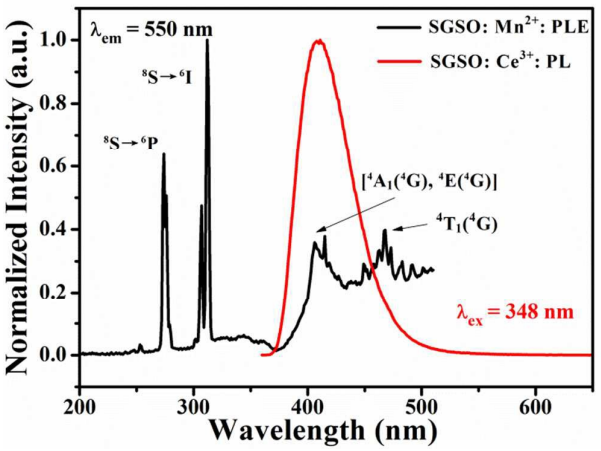

Fig. 8 The excitation spectrum of SGSO:Mn^{2+} and the emission spectrum of SGSO:Ce^{3+}.

Mn^{2+} from $^6A_1(^6S)$ to $^4E(^4D)$, $^4T_2(^4D)$, $[^4A_1(^4G), ^4E(^4G)]$, $^4T_2(^4G)$, and $^4T_1(^4G)$, respectively. Moreover, from Fig.8 we could also find that there existed a significant overlap between the excitation spectrum of SGSO:Mn^{2+} (370−460 nm) and emission spectrum of SGSO:Ce^{3+}. As a consequence, there likely had a strong resonant energy transfer between the sensitizer Ce^{3+} and the activator Mn^{2+}.

Inspection of Fig. 9(a) shows the emission spectra of SGSO:0.26Ce^{3+}, zMn^{2+} (z = 0, 0.09, 0.21, 0.33, 0.45, 0.57, 0.69, 0.81) under 348 nm excitation, which showed not only a broad blue band peaked at 416 nm due to the transitions of 5d → 4f of Ce^{3+} but also a green-emitting band (500−650 nm, $^4T_1 \rightarrow {}^6A_1$) of the Mn^{2+} ions. With increasing Mn^{2+} concentration, the emission intensities of Ce^{3+} decreased by degrees, whereas the emission intensities of Mn^{2+} increased at first then decreased with quenching concentration at z = 0.57 (Fig. 9(b)), further reflecting the result of energy transfer from Ce^{3+} to Mn^{2+}.

Similarly, for SGSO:0.26Ce^{3+}, zMn^{2+} (z = 0, 0.09, 0.21, 0.33, 0.45, 0.57, 0.69, 0.81), the lifetime of Ce^{3+} decreased with increasing Mn^{2+} concentration, as 34.9, 33.8, 32.9, 31.9, 30.9, 30.0, 28.5 ns, respectively. Fig. S2 shows that the luminescence lifetime of Ce^{3+} decreases with increasing Mn^{2+} concentration because the energy transfer from Ce^{3+} to Mn^{2+}.

The energy transfer mechanism between the sensitizer (Ce^{3+}) and activator (Mn^{2+}) was also calculated with equation (7). Fig. S3 shows the relationship between $\boldsymbol{I_{S0}/I_S}$ and $\boldsymbol{z^{n/3}}$ in SGSO:0.26Ce^{3+}, zMn^{2+} when n = 6, 8, 10. The curve for $\boldsymbol{I_{S0}/I_S}$ vs. $\boldsymbol{z^{n/3}}$ was closer to a linear relationship when n = 6, and this clearly indicated that the energy transfer between Ce^{3+} and Mn^{2+} was the dipole–dipole mechanism in the SGSO host. The critical distances ($\boldsymbol{R_C}$) calculated by the quenching concentration method was 11.10 Å. All of these results indicated the efficient energy transfer from Ce^{3+} to Mn^{2+}.

3.5 Thermal photoluminescence properties of SGSO:Ce^{3+}, Tb^{3+}/Mn^{2+}

The thermal quenching of phosphors applied in devices is one of the most important technological parameters. The temperature of the devices usually increases to 100–150 °C and even higher, which related to the chromaticity and brightness of phosphors.[2]

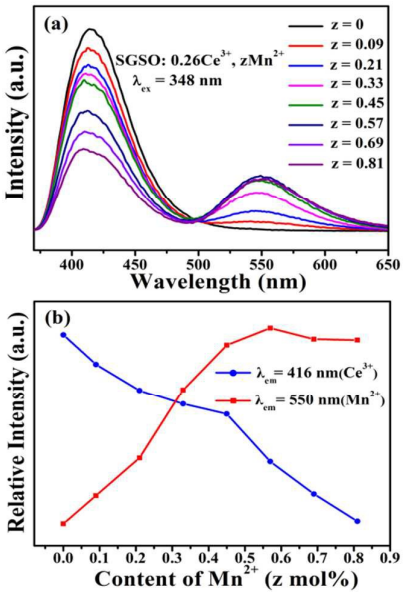

Fig. 9 (a) The emission spectra of SGSO:0.26Ce^{3+}, zMn^{2+} (z = 0, 0.09, 0.21, 0.33, 0.45, 0.57, 0.69, 0.81) under excitation at 348 nm. (b) The emission relative intensity of Ce^{3+} and Mn^{2+}.

Consequently, the thermal photoluminescence stability of devices depends strongly on phosphors. Thus, the temperature dependence emission spectra of SGSO:0.26Ce^{3+} under 348 nm in the temperature range of 25 °C to 200 °C were shown in Fig. 10. It could be seen that the luminescence intensity of Ce^{3+} had an obvious decreasing tendency with increasing temperature, and the luminescence intensity dropped to 62.6% of the initial intensity when the temperature was raised up to 150 °C. The temperature dependent luminescence behavior of SGSO:0.26Ce^{3+}, 0.60Tb^{3+} and SGSO:0.26Ce^{3+}, 0.45Mn^{2+} under 348 nm excitation are also depicted in Fig. 11. The temperature dependence of the integral emissions of Ce^{3+}, Tb^{3+} and Mn^{2+} are also illustrated, respectively. Both the integral intensity of Tb^{3+} emission and that of Mn^{2+}

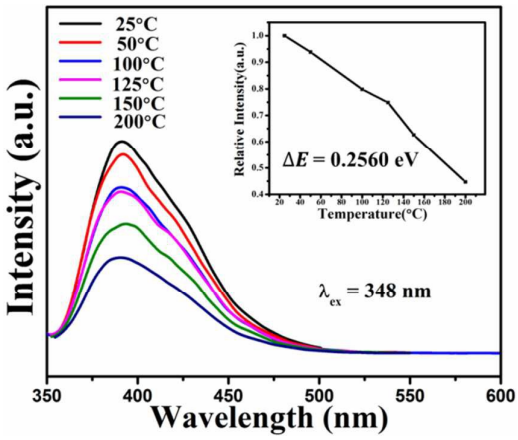

Fig. 10 Temperature-dependent emission spectra of SGSO:0.26Ce^{3+} under different temperatures in the range of 25–200 °C.

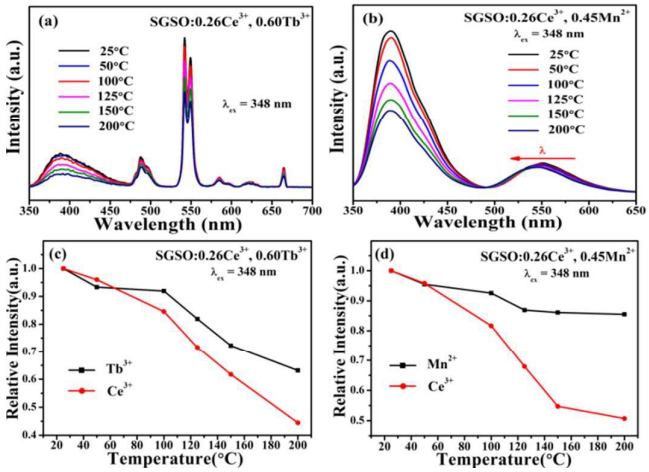

Fig. 11 Temperature-dependent emission spectra of (a) SGSO:0.26Ce^{3+}, 0.60Tb^{3+}, (b) SGSO:0.26Ce^{3+}, 0.45Mn^{2+}. The variations of the relative emission intensities of (c) SGSO:0.26Ce^{3+}, 0.60Tb^{3+}, (d) SGSO:0.26Ce^{3+}, 0.45Mn^{2+}.

decreased more gradually than Ce^{3+} with increasing temperature. The luminescence intensity of Tb^{3+} and Mn^{2+} decreased to 72.3% and 86.1% at 150 °C comparing to room temperature. These phenomena provided the proof that the energy transfer efficiency through $Ce^{3+} \rightarrow Tb^{3+}$ and $Ce^{3+} \rightarrow Mn^{2+}$ was observably influenced by temperature. When Ce^{3+} ion was irradiated by 348 nm light excitation, electron was pumped to the higher component of 5d level, and then relaxed to the lower excited state ($^5D_{3/2}$, ~22,988) of Ce^{3+} ion, and the excited state ($^5D_4$) of Tb^{3+} ion was at ~20,576 cm^{-1}. The difference between the two close levels was about 2412 cm^{-1}. It was reported that the vibration frequency for a perfectly symmetric SiO_4 tetrahedron was about 608 cm^{-1}.[51] Therefore, it was reasonable and probably that the energy difference between the lowest excited state of Ce^{3+} ion and the excited state ($^5D_4$) of Tb^{3+} ion was bridged by the activated phonons in SGSO host. In conclusion, there proposed thermally activated phonon-assisted energy transfer through $Ce^{3+} \rightarrow Tb^{3+}$ in SGSO.[52,53] The same principle could explain the increasing integral intensity ratio of Mn^{2+}/Ce^{3+} with temperature increasing.

To better understand the temperature dependence of photoluminescence, the activation energy (ΔE) was calculated. The activation energy for thermal quenching was estimated using the Arrhenius equation:[54,55]

$$I_T = \frac{I_0}{1+c\exp\left(-\frac{\Delta E}{kT}\right)} \quad (9)$$

where I_0 is the initial emission intensity of the phosphor at room temperature, I_T is the luminous intensity at different temperatures, c is a constant, ΔE is the activation energy for thermal quenching, and k is Boltzmann constant (8.62×10^{-5} eV). According to the equation, the activation energy ΔE could be calculated from a plotting of $\ln[(I_0/I_T)-1]$ against $1/kT$, where a straight slope equals $-\Delta E$. As shown in Fig. 12, ΔE was found to be 0.2013 and 0.1233 eV for Tb^{3+} and Mn^{2+}, respectively. In addition, the ΔE for single doped of

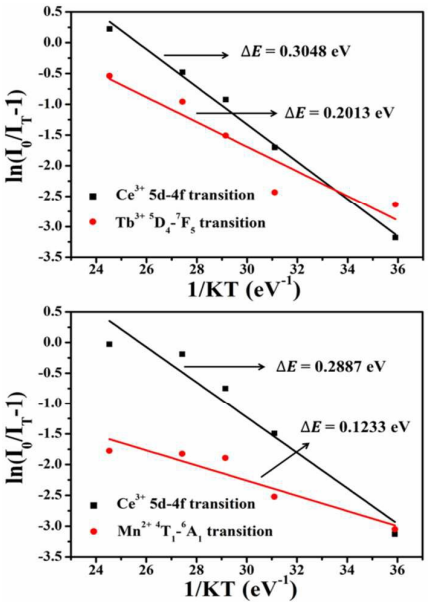

Fig. 12 $\ln[(I_0/I_T)-1]$ versus $1/kT$ plot and the thermal activation energy of SGSO:0.26Ce^{3+}, 0.60Tb^{3+} and SGSO:0.26Ce^{3+}, 0.45Mn^{2+}.

Ce^{3+} as a sensitizer was also investigated. When Ce^{3+} was single doped in SGSO host, the ΔE was calculated to be 0.2560 eV. However, the ΔE of Ce^{3+} increased to 0.3048 eV and 0.2887 eV as co-doping Tb^{3+} and Mn^{2+}. The relatively high activation energy resulted in a good thermal stability for this phosphor. This phenomenon might be ascribed to the weakness of the 5d orbits splitting of Ce^{3+}. When smaller Tb^{3+} or Mn^{2+} ions substituted the larger Gd/Sr sites, the crystal structure became looser, resulting in the slackness of crystal field strength around Ce^{3+}. To express the variation of ΔE of Ce^{3+} more vividly, the configurational coordinate diagram of the ground state of Ce^{3+} and the excited states of Ce^{3+} is exhibited in Fig. 13. Under the 348 nm light excitation, the electrons were excited to the excited states from the ground to $^5D_{3/2}$. At the room temperature, most of the electrons returned to the ground

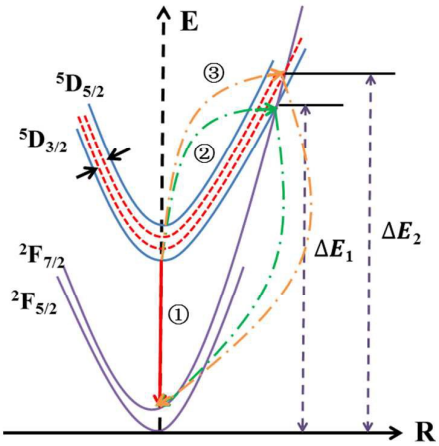

Fig. 13 The configurational coordinate diagram of the ground states and the excited states of Ce^{3+}.

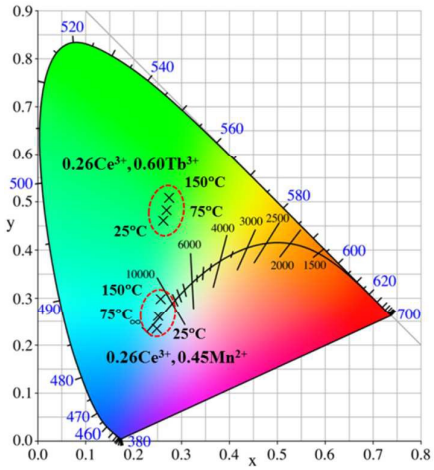

Fig. 14 The CIE chromaticity coordinates as a function of temperature of the SGSO:0.26Ce^{3+}, 0.60Tb^{3+} and SGSO:0.26Ce^{3+}, 0.45Mn^{2+}.

state along the way ①, which emitted light. But with the increased of temperature, most electrons absorbing activation energy ΔE returned to the ground along the way ②, which was the non-radiative transition. Here, the energy difference between $^5D_{3/2}$ and $^5D_{5/2}$ became narrower due to the change of crystal field strength around Ce^{3+}. As a consequence, after absorbing activation energy ΔE, most electrons returned to the ground along the way ③. The co-doping of Tb^{3+} or Mn^{2+} provided a hard way for electrons returning to the ground state, which was the reason for the higher thermal stability of Ce^{3+}. Additionally, with the integral intensity of Tb^{3+} or Mn^{2+} decreased more gradually than Ce^{3+} by increasing temperature, the CIE chromaticity coordinates shifted to green region with increasing temperature, as shown in Fig. 14. However, the emission

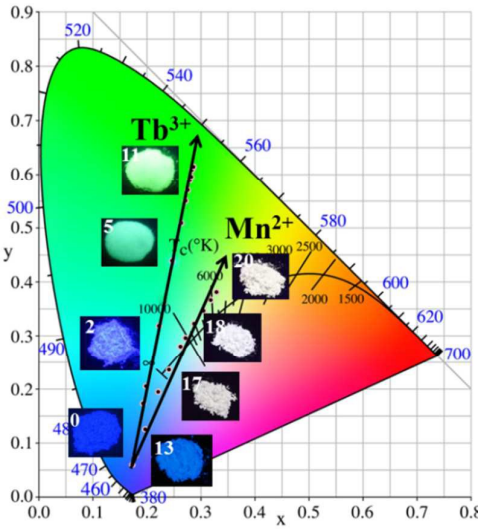

Fig. 15 The CIE chromaticity coordinates diagram for SGSO:0.26Ce^{3+}, yTb^{3+} (y = 0, 0.02, 0.06, 0.10, 0.20, 0.40, 0.60, 0.80, 1.00, 1.20, 1.40, 1.60, 1.74) and SGSO:Ce^{3+}, zMn^{2+} (z = 0, 0.09, 0.21, 0.33, 0.45, 0.57, 0.69, 0.81).

Table 2 The CIE chromaticity coordinates (x, y) and QYs of SGSO:0.26Ce^{3+}, yTb^{3+} (y = 0, 0.02, 0.06, 0.10, 0.20, 0.40, 0.60, 0.80, 1.00, 1.20, 1.40, 1.60, 1.74) and SGSO:Ce^{3+}, zMn^{2+} (z = 0, 0.09, 0.21, 0.33, 0.45, 0.57, 0.69, 0.81).

No.	Composition	CIE(X, Y)	QYs (%)
0	SGSO:0.26Ce^{3+}	0.174, 0.060	60.2
1	SGSO:0.26Ce^{3+}, 0.02Tb^{3+}	0.174, 0.060	25.8
2	SGSO:0.26Ce^{3+}, 0.06Tb^{3+}	0.193, 0.173	33.2
3	SGSO:0.26Ce^{3+}, 0.10Tb^{3+}	0.199, 0.205	80.2
4	SGSO:0.26Ce^{3+}, 0.20Tb^{3+}	0.222, 0.318	68.6
5	SGSO:0.26Ce^{3+}, 0.40Tb^{3+}	0.232, 0.363	62.8
6	SGSO:0.26Ce^{3+}, 0.60Tb^{3+}	0.263, 0.510	47.7
7	SGSO:0.26Ce^{3+}, 0.80Tb^{3+}	0.272, 0.550	50.2
8	SGSO:0.26Ce^{3+}, 1.00Tb^{3+}	0.276, 0.571	52.1
9	SGSO:0.26Ce^{3+}, 1.20Tb^{3+}	0.280, 0.590	76.3
10	SGSO:0.26Ce^{3+}, 1.40Tb^{3+}	0.282, 0.596	59.6
11	SGSO:0.26Ce^{3+}, 1.60Tb^{3+}	0.284, 0.609	54.8
12	SGSO:0.26Ce^{3+}, 1.74Tb^{3+}	0.286, 0.615	56.6
13	SGSO:0.26Ce^{3+}, 0.09Mn^{2+}	0.178, 0.076	55.2
14	SGSO:0.26Ce^{3+}, 0.21Mn^{2+}	0.198, 0.123	44.0
15	SGSO:0.26Ce^{3+}, 0.33Mn^{2+}	0.222, 0.195	61.3
16	SGSO:0.26Ce^{3+}, 0.45Mn^{2+}	0.241, 0.236	60.8
17	SGSO:0.26Ce^{3+}, 0.57Mn^{2+}	0.263, 0.280	62.4
18	SGSO:0.26Ce^{3+}, 0.69Mn^{2+}	0.272, 0.296	51.5
19	SGSO:0.26Ce^{3+}, 0.81Mn^{2+}	0.287, 0.323	42.1
20	SGSO:0.26Ce^{3+}, 0.93Mn^{2+}	0.306, 0.347	—
21	SGSO:0.26Ce^{3+}, 1.05Mn^{2+}	0.319, 0.367	—

color still located in a small region from 25 °C to 200 °C, as given in the dashed red circles in the CIE diagram. The same phenomenon was found from the previous report Ref. [47].[47]

3.6 QYs and CIE of SGSO:Ce^{3+}, Tb^{3+}/Mn^{2+}

QYs is defined as the ratio of the number of photons emitted to the number of photons absorbed in unit time. For solid state lighting applications, the QY is an important parameter to be considered. To accurately investigate the luminescence properties of phosphors, the QYs of SGSO:Ce^{3+}, Tb^{3+}/Mn^{2+} phosphors under 348 nm UV excitation were measured and listed in Table 2. It could be seen that the QYs of Ce^{3+} single doped SGSO phosphor was 60.2%. However, when Tb^{3+} or Mn^{2+} was co-doped with Ce^{3+} in the SGSO host, the QYs of SGSO:Ce^{3+}, Tb^{3+}/Mn^{2+} decreased firstly with the increase of Tb^{3+} or Mn^{2+} content which indicating the $Ce^{3+} \rightarrow Tb^{3+}$ and $Ce^{3+} \rightarrow Mn^{2+}$ energy transferred happen in SGSO host. The maximum QYs of as-prepared SGSO:Ce^{3+}, Tb^{3+} samples could reach 80.2% at y = 0.10, which demonstrated that efficient energy transfer could occur

between Ce^{3+} and Tb^{3+} ions. Moreover, by optimizing the experimental conditions and the compositions of the phosphors, the QYs could be improved. The energy transfer from sensitizer to activator was a viable route to realize color-tunable emission in single host, and a white light emission could be obtained through adjusting the concentration of sensitizer and activator at a suitable ratio. In this SGSO:Ce^{3+}, $y$$Tb^{3+}$/$z$$Mn^{2+}$ system, it was hopeful to realize color-tunable emission even white light emission through energy transfer due to the blue and green emission of Ce^{3+}, Tb^{3+} and Mn^{2+}. Thereby, the CIE chromaticity coordinate of SGSO:Ce^{3+}, $y$$Tb^{3+}$/$z$$Mn^{2+}$ (y = 0, 0.02, 0.06, 0.10, 0.20, 0.60, 0.80, 1.00, 1.20, 1.40, 1.60, 1.74) (z = 0, 0.09, 0.21, 0.33, 0.45, 0.57, 0.69, 0.81) phosphors under 348 nm excitation which were calculated based on the corresponding emission spectra is showed in Fig. 15. From the representing features of chromaticity coordinates above, we could find that the color tone of the SGSO:Ce^{3+}, $y$$Tb^{3+}$ (y = 0, 0.02, 0.06, 0.10, 0.20, 0.60, 0.80, 1.00, 1.20, 1.40, 1.60, 1.74) phosphors shifted gradually from blue to green position with the increasing of Tb^{3+} concentration. The color hue of SGSO:Ce^{3+}, $z$$Mn^{2+}$ (z = 0, 0.09, 0.21, 0.33, 0.45, 0.57, 0.69, 0.81) phosphors changed from blue to near white region with the increase of z values. In order to have a more intuitive expression for the emission colors of our prepared samples, the digital photographs taken under a 365 nm UV lamp are also shown in Fig. 15. Based on these results, the obtained phosphors could act as potential color tunable phosphors for its possible applications in solid-state lighting and display.

4. Conclusion

In summary, we have successfully developed novel bluish-green-white tunable emitting SGSO:Ce^{3+}, Tb^{3+}/Mn^{2+} phosphors by the conventional solid-state reaction. For the samples doped with only Ce^{3+} ions, an asymmetric emission spectrum peaking at 416 nm was observed due to the 4*f*–5*d* transition of Ce^{3+}, and the optimal concentration was 0.26. When Ce^{3+} and Tb^{3+}/Mn^{2+} ions were co-doped into the host, the spectroscopic data of SGSO:Ce^{3+}, SGSO:0.26Ce^{3+}, $y$$Tb^{3+}$ (y = 0.02, 0.06, 0.10, 0.20, 0.40, 0.60, 0.80, 1.00, 1.20, 1.40, 1.60, 1.74) and SGSO:Ce^{3+}, $z$$Mn^{2+}$ (z = 0, 0.09, 0.21, 0.33, 0.45, 0.57, 0.69, 0.81) indicated that the Ce^{3+} to Tb^{3+} or Mn^{2+} energy transfer process occurred in the SGSO host under near-UV excitation. The Ce^{3+} to Tb^{3+} or Mn^{2+} energy transfer in SGSO phosphors were demonstrated to be a resonant type via the dipole−quadrupole mechanism and dipole−dipole mechanism. Due to the energy transfer from Ce^{3+} → Tb^{3+} and Ce^{3+} → Mn^{2+}, both the integral intensity of Tb^{3+} emission and that of Mn^{2+} decreased more gradually than Ce^{3+} with increasing temperature. The luminescence intensity of Tb^{3+} and Mn^{2+} decreased to 72.3% and 86.1% at 150 °C comparing to room temperature. Compared to single doped Ce^{3+}, the co-doping of Tb^{3+} or Mn^{2+} resulted in the higher thermal stability of Ce^{3+} because Tb^{3+} or Mn^{2+} ions provided a hard way for electrons returning to the ground state of Ce^{3+}. And the QYs of the SGSO:0.26Ce^{3+}, 0.10Tb^{3+} and SGSO:0.26Ce^{3+}, 0.57Mn^{2+} phosphors reached 80.2% and 62.4% under the excitation of 348 nm. The emission color of SGSO:0.26Ce^{3+}, $y$$Tb^{3+}$ (y = 0.02, 0.06, 0.10, 0.20, 0.40, 0.60, 0.80, 1.00, 1.20, 1.40, 1.60, 1.74) and SGSO:Ce^{3+}, $z$$Mn^{2+}$ (z = 0, 0.09, 0.21, 0.33, 0.45, 0.57, 0.69, 0.81) phosphors tuned from deep blue to green and white via controlling the concentration of Tb^{3+} or Mn^{2+}. These results indicate that these novel phosphors would be single-phase color-tunable phosphors for ultraviolet-convertible devices.

Acknowledgements

This work was supported by the National Natural Science Foundation of China (Grant Nos. 21571162, 21171152, 21301162), the Guangdong Province Enterprise-University-Academy Collaborative Project (No. 2012B091100474) and Open Foundation of Hubei key laboratory of low dimensional optoelectronic materials and devices (No. HLOM142002).

References

1 X.F. Li, J.D. Budai, F. Liu, J.Y. Howe, J.H. Zhang, X.J. Wang, Z.J. Gu, C.J. Sun, R.S. Meltzer and Z.W. Pan, Light-Sci. Appl., 2013, **2**, 1.
2 H.K. Liu, Y. Luo, Z.Y. Mao, L.B. Liao and Z.G. Xia, J. Mater. Chem. C, 2014, **2**, 1619.
3 C.H. Huang, T.M. Chen, W.R. Liu, Y.C. Chiu, Y.T. Yeh and S.M. Jang, ACS Appl. Mater. Inter., 2010, **2**, 259.
4 N. Guo, Y.J. Huang, H.P. You, M. Yang, Y.H. Song, K. Liu and Y.H. Zheng, Inorg. Chem., 2010, **49**, 10907.
5 J.S. Hou, W.Z. Jiang, Y.Z. Fang and F.Q. Huang, J. Mater. Chem. C, 2013, **1**, 5892.
6 T. Pulli, T. Dönsberg, T. Poikonen, F. Manoocheri, P. Kärhä and E. Ikonen, Light-Sci. Appl., 2015, **4**, 332.
7 Z.G. Xia, C.G. Ma, M.S. Molokeev, Q.L. Liu, K. Rickert and K.R. Poeppelmeier, J. Am. Chem. Soc., 2015, **137**, 12494.
8 J. Zhou, Z.G. Xia, M.Y. Chen, M.S. Molokeev and Q.L Liu, SCI REP-UK, 2015, **5**, 12149.
9 A.A. Setlur, W.J. Heward, M.E. Hannah and U. Happek, Chem. Mater., 2008, **20**, 6277.
10 Y.F. Liu, X. Zhang, Z.D. Hao, X.J. Wang and J.H. Zhang, J. Mater Chem., 2011, **21**, 6354.
11 X.F. Zhou, Z.Y. Zhang and Y.H. Wang, J. Mater. Chem. C, 2015, **3**, 3676.
12 Q.F. Guo, L.B. Liao and Z.G. Xia, J. Lumin., 2014, **145**, 65.
13 Y.M. Feng, J.P. Huang, L.L. Liu, J. Liu and X.B. Yu, Dalton Trans., 2015, **44**, 15006.
14 W.Z. Lv, N. Guo, Y.C. Jia, Q. Zhao and H.P. You, Opt. Mater., 2013, **35**, 1013.
15 J. Zhou, Z.G Xia, H.P. You, K. Shen, M.X. Yang and L.B. Liao, J. Lumin., 2013, **135**, 20.
16 B.H. Li, J. Yang, J. Wang and M.M. Wu, Opt. Mater., 2014, **36**, 1649.
17 M.F. Zhang, Y.J. Liang, Z.G. Xia, F. Yang, D.Y. Yu and G.G. Li, Mater. Res. Bull., 2013, **48**, 4749.
18 Z.G. Xia and W.W. Wu, Dalton Trans., 2013, **42**, 12989.
19 Z.P. Ci, Q.S. Sun, M.X. Sun, X.J. Jiang, S.C. Qin and Y.H. Wang, J. Mater. Chem. C, 2014, **2**, 5850.
20 D.X. Wei, Y. Sun, L.Z. Jiang, S.X. Hu and D. Li, New J. Chem., 2015, **39**, 4753.
21 Y.Y. Li, J.Y. Ding, Q.S. Wu, Q.L., X.C. Wang and Y.H. Wang, J. Mater. Chem. C, 2015, **3**, 8949.
22 C.Y. Cao, H.K. Yang, J.W. Chung, B.K. Moon, B.C. Choi, J.H. Jeong and K.H. Kim, J. Mater. Chem., 2011, **21**, 10342.
23 B.L. Wang, L.Z. Sun and H.D. Ju, Solid State Commun., 2010, **150**, 1460.
24 H.K. Liu, L.B. Liao and Z.G. Xia, RSC Adv., 2014, **4,** 7288.
25 Z.P. Lian, J.F. Sun, L.J. Zhang, D.Z. Shen, G.Q. Shen, X.Q. Wang and Q.F. Yan, RSC Adv., 2013, **3**, 16534.

26 J.L. Zhang, Y.N. He, Z.X. Qiu, W.L. Zhang, W.L. Zhou, L.P. Yu and S.X. Lian, Dalton Trans., 2014, **43**, 18134.
27 W. Lv, N. Guo, Y.C. Jia, Q. Zhao, W.Z. Lv, M.M. Jiao, B.Q. Shao and H.P. You, Inorg. Chem., 2013, **52**, 3007.
28 C. Peng, G.G. Li, X.J. Kang, C.X. Li and J. Lin, J. Colloid Interface Sci., 2011, **355**, 89-95.
29 H. Nagabhushana, D.V. Sunitha, S.C. Sharma, S.C. Prashantha, B.M. Nagabhushana and R.P.S. Chakradhar, J. Alloys Compd., 2014, **616**, 284.
30 T. Komukai, Y. Takatsuka, H. Kato and M. Kakihana, J. Lumin., 2015, **158**, 328.
31 R. Naik, S.C. Prashantha, H. Nagabhushana, H.P. Nagaswarupa, K.S. Anantharaju, B.M. Nagabhushana, H.B. Premkumar and K.M. Girish, J. Alloys Compd., 2014, **617**, 69.
32 P.J. Wang, X.H. Xu, D.C. Zhou, X. Yu and J.B. Qiu, Inorg. Chem., 2015, **54**, 1690.
33 Y.Q. Li, N. Hirosaki, R.J. Xie, T. Takeda and M. Mitomo, Chem. Mater., 2008, **20**, 6704.
34 A.P. Tyutyunnik, I.I. Leonidov, L.L. Surat, I.F. Berger and V.G. Zubkov, J. Solid State Chem., 2013, **197**, 447.
35 T. Yamanaka and H. Mori, Acta Crystallogr. B, 1981, **37**, 1010.
36 H. Yamane, T. Nagasawa, M. Shimada and T. Endo, Acta Crystallogr. C, 1997, **53**, 1533.
37 C.W. Yeh, W.T. Chen, R.S. Liu, S.F. Hu, H.S. Sheu, J.M. Chen and H.T. Hintzen, J. Am. Chem. Soc., 2012, **134**, 14108.
38 L.G. Van Uitert, J. Lumin., 1984, **29**, 1.
39 J. Zhou and Z.G. Xia, J. Mater. Chem. C, 2015, **3**, 7552.
40 G. Zhu, S.Y. Xin, Y. Wen, Q. Wang, M.D. Que and Y.H. Wang, RSC Adv., 2013, **3**, 9311.
41 B.M. Mothudi, O.M. Ntwaeaborwa, S.S. Pitale and H.C. Swart, J. Alloys Compd., 2010, **508**, 262.
42 M.F. Zhang, Y.J. Liang, R. Tang, D.Y. Yu, M.H. Tong, Q. Wang, Y.L. Zhu, X.Y. Wu and G.G. Li, RSC Adv., 2014, **4**, 40626.
43 F.Y. Xie, J.H. Li, Z.Y. Dong, D.W. Wen, J.X. Shi, J. Yan and M.M. Wu, RSC Adv., 2015, **5**, 59830.
44 Y. Wen, Y.H. Wang, F. Zhang and B.T. Liu, Mater. Chem. Phys., 2011, **129**, 1171.
45 R. Reisfeld, E. Greenberg, R. Velapoldi and B. Barnett, J. Chem. Phys., 1972, **56**, 1698.
46 D.L. Dexter, J. Chem. Phys., 1953, **21**, 836.
47 J. Zhou and Z.G. Xia, J. Mater. Chem. C, 2014, **2**, 6978.
48 J.M.P.J. Verstegen, J.L. Sommerdijk and J.G. Verriet, J. Lumin., 1973, **6**, 425.
49 L. Shi, Y.L. Huang and H.J Seo, J. Phys. Chem. A, 2010, **114**, 6927.
50 J. He, S. Zhang, J.B. Zhou, J.P. Zhong, H.B. Liang, S.S. Sun, Y. Huang and Y. Tao, Opt. Mater., 2015, **39**, 81.
51 R.L. Frost, A. López, Y.F. Xi and R. Scholz, Spectrochim. Acta Part A, 2015, **137**, 717.
52 J.Y. Sun, J.C. Zhu, X.Y. Zhang, Z.G. Xia and H.Y. Du, J. Lumin., 2012, **132**, 2937.
53 H.D. Luo, J. Liu, X. Zheng, L. X. Han, K. X. Ren and X. B. Yu, J. Mater. Chem., 2012, **7**, 15892.
54 J.S. Kim, H.J. Song, H.S. Roh, D.K. Yim, J.H. Noh and K.S. Hong, Mater. Lett., 2012, **79**, 112.
55 J. Zhou and Z.G. Xia, J. Lumin., 2014, **146**, 22.

Graphical Abstract

A series of SGSO:Ce^{3+},Tb^{3+}/Mn^{2+} phosphors have been synthesized via a solid-state reaction. The energy transfer were designed from Ce^{3+} to Tb^{3+} or Mn^{2+}, which can modulate emission colors from blue to green and near white, and enhance their luminescence intensity for possible applications as ultraviolet-convertible phosphors.